

POREMAPS: A FINITE DIFFERENCE BASED POROUS MEDIA ANISOTROPIC PERMEABILITY SOLVER FOR STOKES FLOW

David Krach^{1,2} , Matthias Ruf¹, Holger Steeb^{1,2}

¹Institute of Applied Mechanics (CE), University of Stuttgart, Stuttgart, Germany; ²Stuttgart Center for Simulation Science, University of Stuttgart, Stuttgart, Germany

Correspondence to: David Krach,

david.krach@mib.unistuttgart.de

How to Cite:

Krach, D., Ruf, M., & Steeb, H. POREMAPS: A finite difference based Porous Media Anisotropic Permeability Solver for Stokes flow. *InterPore Journal*, 2(1), IPJ260225–7.

https://doi.org/10.69631/ipj.v2i1nr39

RECEIVED: 30 July 2024 ACCEPTED: 27 Nov. 2024 PUBLISHED: 26 Feb. 2025

ABSTRACT

Porous materials are ubiquitous in various engineering and geological applications, where their permeability plays a critical role in viscous fluid flow and transport phenomena. Understanding and characterizing the microscale properties, the effective hydraulic parameters, and the anisotropy of porous materials are essential for the accurate modeling and predicting of fluid flow behavior. This study pursues the Digital Rock Physics approach to retrieve intrinsic permeability and its evolution in anisotropic configurations of porous media, which are subjected to pore space alterations. Therefore, we discuss the development and implementation of a computational framework based on the finite difference method to solve the pseudo-unsteady Stokes equations for fluid flow on the pore scale. We present an efficient and highly parallelized implementation of this numerical method for large voxel-based data sets originating from different image-based experimental setups. A comprehensive variety of benchmarks has been conducted to assess and evaluate the performance of the proposed solver. The solver's compatibility with huge domain sizes generated by state-of-the-art imaging techniques is demonstrated. We investigate an open-cell foam undergoing deformation, observing that contrary to initial expectations, no anisotropy emerges. Further, we examine a microfluidic cell experiencing precipitation within its pore space, resulting in clear anisotropic development during the clogging process.

KEYWORDS

Pore-scale resolved modeling, Digital Rock Physics, Permeability, Finite Difference Method, Anisotropy, Micro X-Ray Computed Tomography (µXRCT)



This is an open access article published by InterPore under the terms of the Creative Commons Attribution-NonCommercial-NoDerivatives 4.0 International License (CC BY-NC-ND 4.0) (https://creativecommons.org/licenses/by-nc-nd/4.0/).

Krach, et al Page 2 of 21

1. INTRODUCTION

Experimental investigations and numerical simulations of fluid flow through porous materials with a large variety of hydro-mechanical properties are of interest in many fields such as hydrosystems modeling, groundwater flow and contaminant transport (7, 24), oil reservoir exploitation (4, 14), and industrial applications such as membranes for water desalination (54). The majority of all investigations operate at the macro, i.e., Darcy scale, and use a coarse-grained continuum theory, which means that individual pore geometries are not physically resolved. Furthermore, the correlation between viscous fluid flow and corresponding driving force is assumed to be linear. Porosity ϕ and the intrinsic permeability tensor $\mathbf{k} = k_{ij}\mathbf{e}_i \otimes \mathbf{e}_j$ serve as input parameters for these models. Flow regimes where the components of the permeability tensor k_{ij} do not linearly depend on the driving force are denoted as non-Darcian and are beyond the scope of this contribution. In general, ϕ and effective hydraulic properties like \mathbf{k} of the porous material are highly sensitive to the distinct porous microstructure. This work primarily centers on the assessment and determination of the intrinsic permeability tensor \mathbf{k} .

1.1. State of the Art

There are numerous experimental, semi-analytical and numerical methodologies for permeability determination documented in the literature. Given the expense and complexity of flow experiments and their limitations, as well as the limited applicability of semi-analytical models, it is preferable to assess these parameters with computer simulations. Advances in three-dimensional (3D) imaging techniques, such as micro X-Ray Computed Tomography (μXRCT), along with the widespread availability of suitable devices (45, 62, 63, 64) enable the full resolution of 3D pore geometries. This development allows the flow problem to be directly solved at the pore scale for various porous materials (11). Moreover, twodimensional (2D) data, e.g., generated from images of microfluidic experiments acquired by optical microscopy, extended in the third spatial direction, can provide further input data (27, 60). Deformation of the pore space or precipitation and a corresponding decrease in porosity have a direct influence on the hydro-mechanical properties of a material. Certainly, the process of experimentally determining anisotropic permeability during an experiment is inherently intricate. Acquiring the complete permeability tensor \mathbf{k} is mostly impossible. Nonetheless, this investigation is particularly significant due to the non-trivial implications of deformation or precipitation on the principal directions of hydraulic properties or the material's anisotropic characteristics. In the literature, numerical solvers are applied to porous materials undergoing changes in pore space, cf. for geochemical alteration like calcite precipitation (40), carbonate precipitation for carbon capture and storage applications (30) or external strain causing deformation (5, 25). Another field of interest is the benchmark of specially designed materials whereby the permeability can be controlled via the manufacturing parameters on Al-Cu alloys (9). Due to the limitations of experimentally viable boundary conditions, e.g. undrained boundary conditions along the cylinder of the sample in conventional triaxial cells, a priori assumption must be made for the orientation of principal directions of k. The utilization of the aforementioned imaging techniques combined with computer simulations provides a way for achieving pore-scale resolved computation of all coefficients of the permeability tensor in a systematic way while circumventing any priori assumption. However, to determine changes in anisotropy or computing porosity-permeability relationships, for example, many data points and correspondingly many individual simulations are required. While various numerical methods like Finite Element Method (FEM) (12, 16), Finite Volume Method (FVM) (16, 35) and Lattice-Boltzmann Methods (LBM) (12, 36), Smoothed Particle Hydrodynamics (SPH) (41, 53, 26) or Pore Network Modeling (PNM) (10, 20, 43) have been employed to simulate pore-scale fluid flow, each method comes with its own set of limitations and advantages. In this work, we present an efficient and reliable solver for the Stokes equations by implementing a Finite Difference Method (FDM) based algorithm. In terms of numerical efficiency, the solver is tuned for voxelbased Cartesian grids as directly obtained from image-based characterization methods like µXRCT or microfluidics. It stands out as a versatile and well-established choice due to its straightforward implementation and suitability for complex geometries (1, 8, 21, 34, 42). In addition, FDM is a simple Krach, et al Page 3 of 21

approach in terms of the algorithm, has advantages when using regular grids, and can be effectively parallelized due to its local nature.

1.2. Objective

We aim to develop a resilient and modular open-source tool that advances our comprehension of fluid flow at the pore scale and addresses the issue of evolving anisotropies in porous media under varying conditions. The software tool should be able to handle state-of-the-art data sets from µXRCT scans (up to 2000³ voxels) on various computing architectures and should allow for further extensions. Besides research codes that do not allow for further extensions (only executable of the software available (21)) or commercial solvers such as GeoDict (38), there are common open-source packages such as OpenFoam, e.g. used in Icardi, Boccardo, Marchisio, Tosco, and Sethi (29); Guibert, Horgue, Debenest, and Quintard (22), which are extremely flexible, however these are not tuned for the mentioned demands. Others, such as the tool from the National Institute for Standards and Technology (8), which is written in Fortran, are not multi-node parallelized. The rationale behind developing a new solver, despite the existence of current solutions, is multilayered. We present a fully open-source, platformindependent FDM solver that relies exclusively on the Message Passing Interface (MPI). This solver operates directly on binarized datasets, making it an essential tool for porous media research. Moreover, its full integration into existing experimental setups streamlines the research process, promoting a more cohesive and comprehensive approach to investigating complex phenomena. Since large domains (state-of-the-art µXRCT data sets comprise up to 10^9-10^{10} voxels) must be simulated, in combination with several snapshots for time-resolved investigations, the efficiency and performance as well as the simplicity of the presented FDM solver, is the main focus. The code is written in procedural, functional C++ and is parallelized with the MPI to run on multi-node, multi-core CPU systems.

1.3. Structure

For these reasons, in addition to the permeability determination derivation (Sec. 2), the mathematical basics (Sec. 3), and the numerical principles (Sec. 4), it is particularly important for us to address the implementation and technical aspects (Sec. 5) as well as to provide a detailed validation against various benchmark cases (Sec. 6). In Section 7, we demonstrate the developed solver's ability to investigate two distinct materials characterized by alterations in their pore space. These alterations are anticipated to result in changes not only in the magnitude of the permeability but also in the permeability anisotropy ratio. Specifically, our study focuses on an open-cell foam, which defies expectations by not exhibiting anisotropy as it undergoes deformation. Additionally, we investigate a porous microstructure exposed to mineral precipitation and subsequently clogging, revealing a development of anisotropy that is notably influenced by the boundary conditions of the underlying experiment.

2. PERMEABILITY TENSOR AND PRINCIPAL PERMEABILITIES

Permeability is defined as a proportionality factor between the pressure gradient across the examined sample and fluid fluxes (grad $p \propto \mathbf{q}$). For homogeneous materials that are known to have isotropic material behavior, a scalar value is used for the hydraulic permeability. Intrinsic permeability quantifies viscous losses in continuum-based Darcy-type models. In the generic case, the effective permeability \mathbf{k} is a second order tensor (**Eq. 1**):

$$\mathbf{k} = k_{ij} \ \mathbf{e}_i \otimes \mathbf{e}_j = \begin{bmatrix} k_{11} & k_{12} & k_{13} \\ k_{21} & k_{22} & k_{23} \\ k_{31} & k_{32} & k_{33} \end{bmatrix} \mathbf{e}_i \otimes \mathbf{e}_j$$
 (1)

Here k_{ij} are the components of the coefficient matrix and the Cartesian basis vectors \mathbf{e}_i build the tensorial basis through its dyadic product. Boldface is employed to represent tensors and vectors, with the implicit assumption that equations in index notation abide by Einstein's summation convention. The coefficient matrix is symmetric and positive definite (7, 50). In contrast to the experimental determination of permeability, the numerical approach is capable of computing secondary diagonal elements of k_{ij} ,

Krach, et al Page 4 of 21

which is required for a complete hydraulic characterization. Solving the characteristic polynomial $\det(\mathbf{k}-\lambda\mathbf{I})=0$ for the eigenvalues λ_i (also referred to principal permeabilities k_I,k_{II},k_{III}) we obtain the permeability tensor in its spectral form (**Eq. 2**) expressed in a basis system with the principle axes $\tilde{\mathbf{e}}_i$, that are computed by solving $(\mathbf{k}-\lambda_i\mathbf{I})\cdot\tilde{\mathbf{e}}_i=\mathbf{0}$. **I** is the second order identity tensor.

$$\mathbf{k} = \sum_{i=1}^{3} \lambda_i \ \tilde{\mathbf{e}}_i \otimes \tilde{\mathbf{e}}_i \tag{2}$$

The orientation of the principal axes with respect to the basis system \mathbf{e}_i is computed via the rotation tensor $\mathbf{R} = R_{ik}(\mathbf{e}_i \otimes \mathbf{e}_k)$ whereby $\tilde{\mathbf{e}}_i = \mathbf{R} \cdot \mathbf{e}_i$ and $R_{ki} = \cos \sphericalangle(\mathbf{e}_k, \tilde{\mathbf{e}}_i)$ hold. Determining the principal permeabilities enables categorization of the material into one of the following classes:

1. **Isotropy**: $k_I = k_{II} = k_{III}$

Same hydraulic properties in all three principal directions.

2. Orthotropy: $k_I \neq k_{II} \land k_I \neq k_{III} \land k_{II} \neq k_{III}$

Unique and independent hydraulic properties in three mutually perpendicular directions.

3. Transverse anisotropy: $k_I \neq k_{II} = k_{III} \ \lor \ k_I = k_{III} \neq k_{III} \ \lor \ k_I = k_{III} \neq k_{III}$

Same hydraulic properties in one plane. Thus, there are two independent constants in the permeability tensor. Typical examples of this material are wood, unidirectional fiber composites or sedimentary sandstones.

3. GOVERNING EQUATIONS ON THE PORE SCALE

Pore scale refers to the length scale at which individual pores and their geometrical features, such as pore size and shape, are significant. At this scale, the fluid flow pattern is strongly influenced by the morphology of the pores, as well as the viscous momentum interactions between the fluid phase and the solid skeleton. Pore-scale simulations are used to study fundamental aspects of porous media flow as well as the determination of properties used in coarse-grained Darcy scale methods. We are interested in calculating the intrinsic effective permeability, and therefore consider solving for fluid flow under stationary creeping flow conditions. Accordingly, the following applies for the Reynolds number (Eq. 3) and the fundamental equations to be solved are the Stokes equations consisting of the balance of linear momentum for an incompressible Newtonian fluid (42) (Eq. 4) and the balance of mass (Eq. 5) where ρ , ρ_0 , \mathbf{v} , μ , p, \mathcal{V} , \mathcal{L} are the fluid density, the rest density of the fluid, fluid velocity vector, (constant) dynamic viscosity of the fluid, pore fluid pressure and the characteristic velocity and length, respectively.

$$Re = \frac{\rho_0 V \mathcal{L}}{\mu} < 1 \quad [-]$$

$$\mathbf{0} = \mu \operatorname{div}(\operatorname{grad} \mathbf{v}) - \operatorname{grad} p \tag{4}$$

$$\operatorname{div} \mathbf{v} = 0 \tag{5}$$

No body force is used. In addition to characteristic properties, indicated by notation in script typestyle, to scale for physical quantities we denote dimensionless variables and operators by $(\cdot)^*$. It is well known that solving for **Equation 4** and **Equation 5** causes problems due to the special role of pressure. Therefore, this set of governing equations is extended with an artificial time derivative and a so-called pseudo-unsteady method (42). In this manner, for the numerical implementation, we do not fulfill the incompressibility condition as an algebraic constraint. Instead, an artificial compressibility formulation will be considered with an equation of state for the fluid pressure $p(\rho)$. Hence, we obtain for the nondimensional equations to be solved (**Eq. 6**), where c^* is the dimensionless speed of sound, also

Krach, et al Page 5 of 21

referred to as the artificial compressibility parameter, and dimensionless time derivatives are indicated by (*).

$$\rho^*(\mathbf{v}^*) = \frac{1}{\text{Re}} \operatorname{div} \operatorname{grad}(\mathbf{v}^*) - \operatorname{grad}(p^*) \quad \text{and} \quad (p^*) = -c^{*2} \operatorname{div}(\mathbf{v}^*)$$
 (6)

This numerical approach solves the steady-state Stokes equations by transforming them into a pseudo-time dependent problem which is feasible when dealing with low Reynolds number fluid flows in porous media. It provides a computationally efficient alternative to directly solving the steady-state equations and it can be shown that the solution converges for $t \to \infty$ to the steady-state solution of the original problem (17, 21, 42). The detailed non-dimensionalization with introduction of all quantities, dimensionless differential operators, and the constitutive equations can be found in **Appendix B** (Available online).

4. FINITE DIFFERENCE SCHEME FOR STOKES EQUATIONS

4.1. Simulation parametrization

We introduce the reference length $\mathcal{L}=1$ vx (voxel) and the reference velocity $\mathcal{V}=\frac{1\text{vx}}{\text{s}}$. As the driving force, a constant pressure gradient across the domain is employed with the initial condition $\text{gr}^*\text{ad}(p^*)=\frac{1}{\text{vx}}$. Furthermore, there is no body force present ($\mathbf{b}=\mathbf{0}$). We require a small Reynolds number and fix Re = 0.01 and $c^{*2}=1.5\times10^6$ as in Bentz and Martys (8). Note that the dimension $c^{*2}\approx10^6$ fits well to the physical ratio of the speed of sound in water to the assumed characteristic velocity of creeping flow conditions.

4.2. Grid

Space is discretized with a central difference stencil on a regular staggered Marker-And-Cell (MAC) grid (23), where fluid velocities are stored on the faces of the cells, while the pressure values are stored at the cell centers. Storing different quantities on different locations within each cell allows for an efficient and accurate computation of the pressure gradients as well as for the exact modeling of no-penetration conditions at the fluid-solid interfaces.

4.3. Boundaries in the numerically considered domain and second order derivatives

For the domain boundaries, we apply periodic boundary conditions to simulate a periodic or repeating behavior of the physical system in a unit cell. Periodic boundary conditions allow for transverse flow which is required for anisotropy investigations. However, it is possible to set no-slip conditions on domain boundaries at lateral surfaces if needed, e.g. to replicate a permeameter experiment. The domain boundary in the direction of the pressure gradient is always periodic for the flow. Fluid-solid boundaries correspond to the pixel boundaries of the binary 3D image, and we use no-slip no-penetration boundary conditions on the interfaces, cf. **Figure 1**. Second-order derivatives perpendicular to the local flow direction are analytically determined based on Taylor series approximations. This ensures that the no-

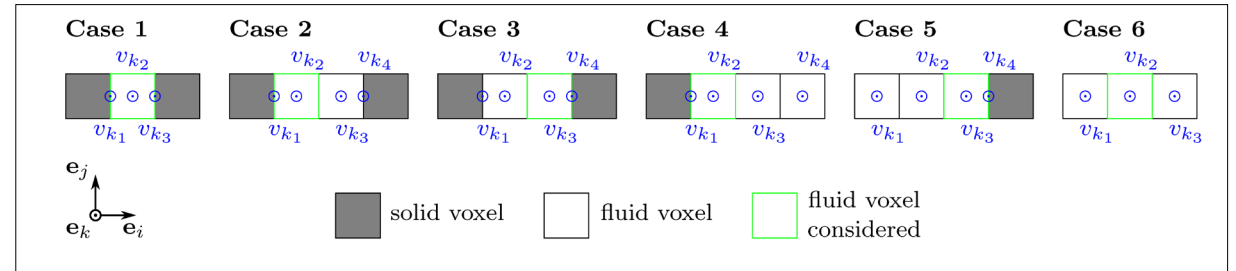


Figure 1: Different cases for the identification of the voxel neighborhood to calculate the second-order derivatives $\left(\frac{\partial^2 v_k}{\partial x_i^2}\right)$ in the perpendicular directions to the considered flow velocity direction for i, j, k = (1, 2, 3), (2, 3, 1), (3, 1, 2).

Krach, et al Page 6 of 21

slip condition is fulfilled on the fluid-solid voxel surfaces. We distinguish six basis cases as in Bentz and Martys (8) and Gerke et al. (21). In **Figure 1** the six distinguished cases are exemplary illustrated for the flow direction \mathbf{e}_k and the perpendicular direction \mathbf{e}_i .

Based on the velocity definitions in **Figure 1**, the second-order derivatives for the different cases can be computed by solving a resulting system of equations. For instance, for case 2, we have a set of three equations to compute $\frac{\partial^2 v_k}{\partial x_i^2}$ as follows (**Eq. 7**):

$$v_{k_{1}} \approx v_{k_{2}} - \frac{1}{2} \frac{\partial v_{k}}{\partial x_{i}} + \frac{1}{8} \frac{\partial^{2} v_{k}}{\partial x_{i}^{2}} - \frac{1}{48} \frac{\partial^{3} v_{k}}{\partial x_{i}^{3}} = 0$$

$$v_{k_{3}} \approx v_{k_{2}} + \frac{\partial v_{k}}{\partial x_{i}} + \frac{1}{2} \frac{\partial^{2} v_{k}}{\partial x_{i}^{2}} + \frac{1}{6} \frac{\partial^{3} v_{k}}{\partial x_{i}^{3}}$$

$$v_{k_{4}} \approx v_{k_{2}} + \frac{3}{2} \frac{\partial v_{k}}{\partial x_{i}} + \frac{9}{8} \frac{\partial^{2} v_{k}}{\partial x_{i}^{2}} + \frac{9}{16} \frac{\partial^{3} v_{k}}{\partial x_{i}^{3}} = 0$$

$$(7)$$

All considered neighborhood cases can be found in the **Appendix C** (Supplementary Material available online).

4.4. Permeability computation

In the so-called creeping flow regime, characterized by low Reynolds numbers, Re < 1.0, it is valid to employ Darcy's law (18) (**Eq. 8**) to compute the entries of the second order permeability tensor where $h_i = -\frac{\partial p}{\partial x_i} = -p_{,i}$ is the pressure gradient and A_i , \bar{A}_i are the total and the effective cross-sectional areas with the normal vectors $\mathbf{n}_i \parallel \mathbf{e}_i$.

$$\mathbf{q} = \frac{1}{\mu} \mathbf{k} \cdot \mathbf{h} \quad \to \quad q_i \mathbf{e}_i = \frac{1}{\mu} k_{ij} (\mathbf{e}_i \otimes \mathbf{e}_j) \cdot h_k \mathbf{e}_k = \frac{1}{\mu} k_{ik} h_k \mathbf{e}_i \quad \text{with} \quad q_i = \frac{1}{A_i} \int_{\partial \mathcal{B}} v_i d\bar{A}_i$$
 (8)

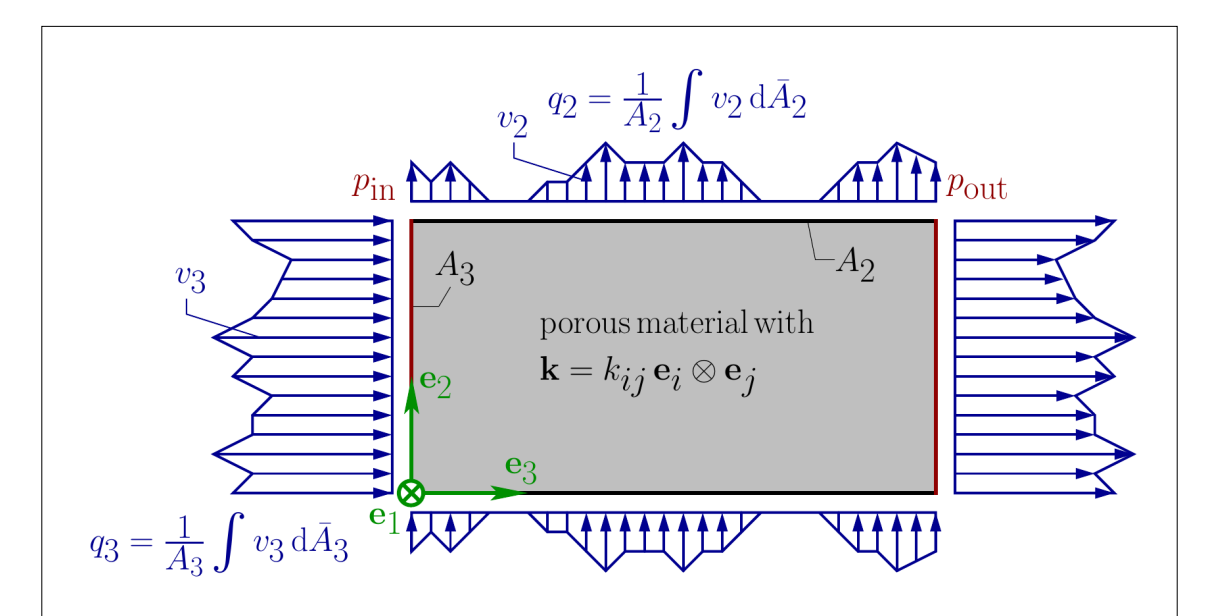


Figure 2: Illustration of the components of Darcy's law with the given boundary values for the pressure $p_{\rm in}$ and $p_{\rm out}$ used to compute the gradient h_3 . Volumetric fluxes q_2 , q_3 are evaluated over the respective boundaries (total and effective cross-sectional areas A_i , $\bar{A_i}$). In ${\bf e}_1$ -direction, the volumetric flux is not shown here, but is handled analogously. With given pressure gradients $h_3 \neq 0$ and $h_1 = h_2 = 0$, this represents case **c**) in **Equation 9**.

Krach, et al Page 7 of 21

In order to determine the nine entries in the coefficient matrix of the permeability tensor, three numerical simulations must be performed. The following pressure gradients h_i are specified for the different simulations (**Eq. 9**), and we measure three fluxes q_i for each case.

a)
$$h_1 \neq 0 \land h_2 = h_3 = 0$$
; **b**) $h_2 \neq 0 \land h_1 = h_3 = 0$; **c**) $h_3 \neq 0 \land h_1 = h_2 = 0$ (9)

For case **c**), all properties are illustrated in **Figure 2**. By comparing the coefficients (**Eq. 8**, right), nine equations are obtained for nine entries of the coefficient matrix of the permeability tensor. A detailed list of the equations for determining the complete permeability tensor **k** can be found in **Appendix D** (Supplementary Material available online).

5. COMPUTATIONAL ASPECTS

5.1. Processing Input Data

Binarized 3D image data (8-bit file format) distinguishing between solid phase and pore space are employed as input for the solver. Commonly performed image pre-processing steps, such as denoising and segmentation, depend on the specific imaging technique and are well-documented in the literature (e.g., Andrä et al. (2, 3); Burger and Burge (13); Iassonov, Gebrenegus, and Tuller (28); Russ and Neal (48); Schlüter, Sheppard, Brown, and Wildenschild (51); Tuller, Kulkarni, and Fink (55)). These steps will not be further elaborated upon here. Depending on the boundary conditions and material, a few pre-processing steps need to be conducted, such as mirroring for symmetric periodicity, domain cropping, or the elimination of disconnected pore spaces. This depends upon the specific problem at hand, a topic that will be delved into within the dedicated application sections. The solver operates under the assumption that the percolation condition is met, meaning that at least one flow path through the material is available.

Algorithm 1: Program Flow Stokes Solver					
Data: Binarized 3D image data					
Initialize MPI;					
Domain decomposition, read partial domains, add halos;					
Impose initial pressure gradient;					
Evaluate neighborhood;					
While $\operatorname{div} \mathbf{v} > \varepsilon \operatorname{do}$					
Compute velocity field $\mathbf{v}_{i,j,k}$;					
Compute pressure field $p_{i,j,k}$;					
If $i \mod CommFrequency \equiv 0$ then					
Communicate halos;					
end					
Compute specific discharge q , see Equation 8 ;					
Evaluate permeability tensor entries $k_{i,j}$, see Equation 8 ;					
Compute convergence criterion $\varepsilon = \frac{\Delta q_3 }{ q_3 }$;					
Write log file;					
end					
Write pressure and velocity fields;					

5.2. Implementation

The solver is completely implemented in C++ and parallelized with OpenMPI (version 4.1.5) (39) to employ it on distributed memory architectures. Special emphasis is put on keeping the code as simple as possible. For the domain decomposition, we use a communicator on a Cartesian topology which is particularly well-suited for regular meshes and 3D geometries. The file IO is fully parallelized and communication between the ranks is executed by blocking send-receive operations. We work directly with binary data which is RAM-efficient and allows for a concise implementation. The source code of POREMAPS is published in Krach, Ruf, and Steeb (32) (Algorithm 1).

Krach, et al Page 8 of 21

The inherent domain decomposition of MPI optimizes communication by embedding the virtual topology onto the physical machine as efficiently as possible, but is not necessarily suitable for domains with high aspect ratios (see Sec. 7.3). Therefore, it is possible to include the desired number of ranks in each direction directly in the input file.

5.3. Scaling

The scalability of FDM codes has been studied extensively in the literature. Several factors contribute to weak scalability, including the communication overhead, memory requirements, and load balancing. For the scaling test we use a 50^3 voxel regular sphere packing per core and the hardware of the experimental compute cluster "ehlers" of the EXC 2075 "SimTech" Cluster of Excellence (University of Stuttgart). The CPU partition is comprised of 8 nodes with 128 cores (2 × 64 cores, AMD EPYC 7702) each and 200 Gb/s Infiniband interconnect and 2 TB of RAM.

The algorithm is very communication heavy. The influence of increasing core-to-core (**Fig. 3**, left) or node-to-node communication (**Fig. 3**, right) causes a decrease in performance. However, as soon as communication in all three spatial directions is required (>8 cores), the computed time steps per second (TPS) are almost constant. Accordingly, the results are satisfactory for the problems at hand. Considering targeted domain sizes, tests beyond 1024 cores are not significant for our applications and therefore not considered here.

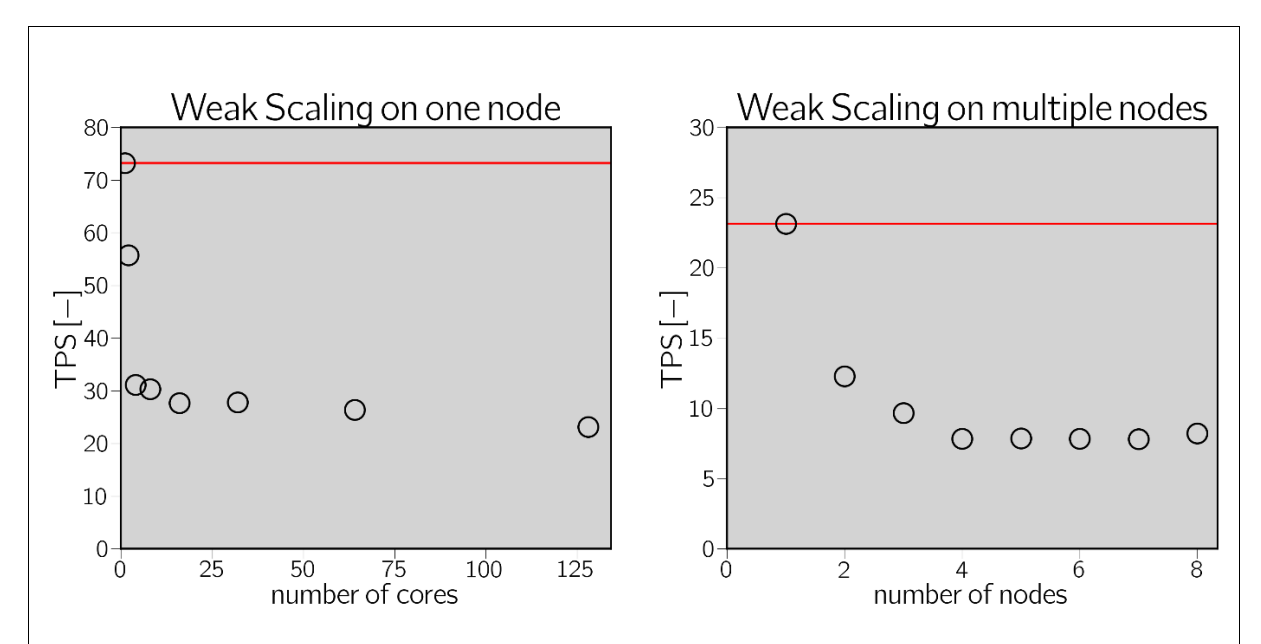


Figure 3: Weak scaling on one node using 1, 2, 4, 8, 16, 32, 64, 128 cores (left) and 1–8 nodes with 128 cores each (right).

6. BENCHMARKS

The code has been designed to facilitate the study of complex, heterogeneous porous materials. To justify the application of the solver to diverse domains, a multi-layered benchmark and validation program is performed with increasing complexity.

- 1) We validate the code against analytical solutions such as Poiseuille flow and channel flow.
- 2) Regular sphere packings with different porosities are considered, for which empirical relationships exist, such as the Kozeny-Carman equation.
- 3) The procedure for determining the anisotropy and the secondary diagonal elements of the permeability tensor is validated.

Krach, et al Page 9 of 21

4) We compare our code with other solvers such as LBM, FEM or mathematical homogenization for different types of porous materials.

6.1. Hagen-Poiseuille Equation

The laminar creeping flow of a Newtonian fluid through a pipe is a standard benchmark for CFD codes. The tube is per definition periodic in direction of the pressure gradient. We compare results for different resolutions and the analytical Hagen-Poiseuille equation presented in Batchelor (6) (Eq. 10) with the radial coordinate r. The length and radius of the tube are $L=0.01\,\mathrm{m}$ and $R=0.001\,\mathrm{m}$. The no-slip condition on the fluid-solid interface results in $v_3(r=R)=0$.

$$v_3(r) = \frac{\Delta p}{4L\mu} (R^2 - r^2) \tag{10}$$

We compare simulation results obtained for different resolutions ($L/dx = \{5, 10, 20, 50, 100\}$) and present the velocity profiles through the center of the tube, see **Figure 4**, left. All resolutions provide very similar solutions and are in agreement with the analytical solution (**Eq. 10**). **Figure 4**, right, gives the cross-section through the tube visualizing the radially symmetric velocity pattern.

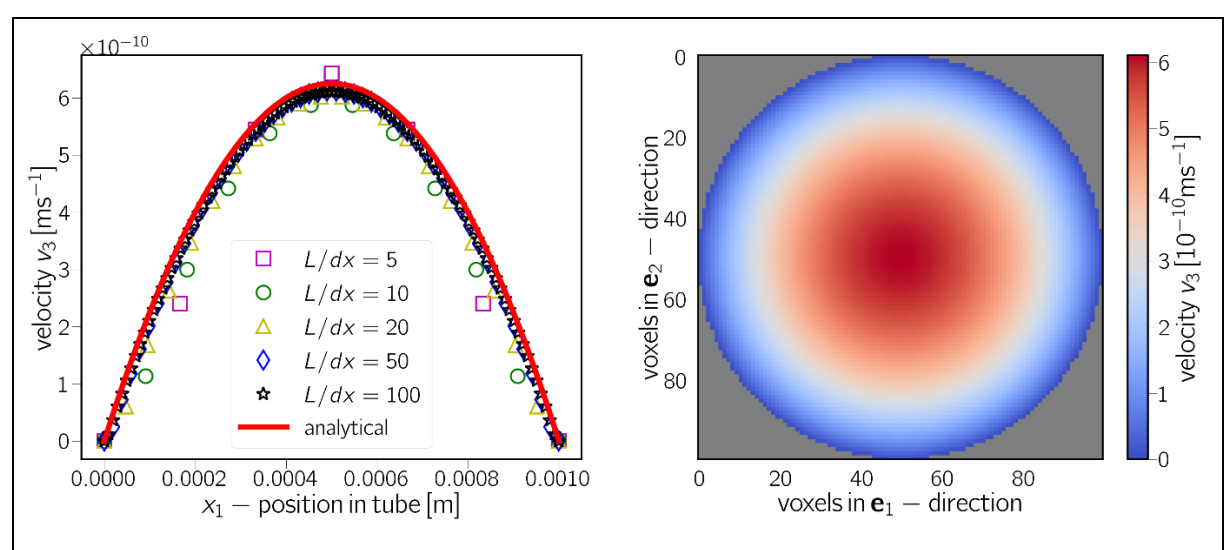


Figure 4: Resolution dependent velocity profiles through a tube compared to the analytical solution (left) and velocity pattern in one cross-section (right).

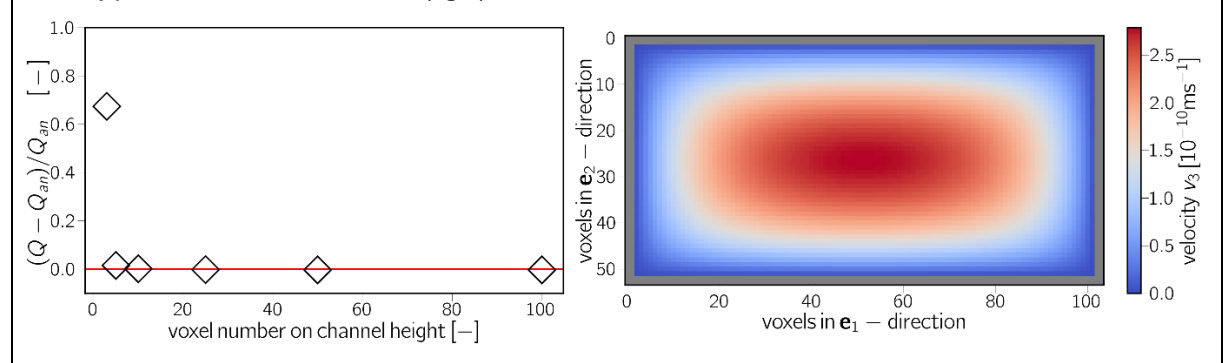


Figure 5: Deviation of the volumetric flux Q from its analytical solution Q_{an} according to White and Majdalani (61) through rectangular cross section channel for different resolutions (left) and corresponding velocity pattern (right).

6.2. Channel Flow - Rectangular Cross Section

To benchmark slightly more complex structures, we analyze the flow through a rectangular channel (Fig. 5). It has an advantage over the tube in **Section 6.1**, since it can be discretized on a cubic lattice without introducing a discretization error. The benchmark provides information about the resolution at

Krach, et al Page 10 of 21

which we can expect valid results from the solver. That is of particular interest for the study of microfluidic experiments in order to resolve the channels sufficiently.

Presented are simulation results for different resolutions ($h/dx = \{3, 5, 10, 25, 50, 100\}$) for the channel height h. The width of the channel equals b = 2h. Already with a resolution of the channel cross-section bigger than 5×10 voxels, the volumetric flow rate Q = qA corresponds with results for higher resolutions (errors of 67 %, 1.5 % for rectangular channels with 5×3 and 10×5 voxels respectively and below 0.1 % for all higher resolutions). Although the solution depends on the discretization, it converges already for low resolutions which is essential for the computation of microfluidic domains.

6.3. Regular Sphere Packings

Due to the periodicity of regular sphere packings, the simulation of flow can be reduced to a cubic unit cell of side-length L. It is therefore possible to simulate representative porous structures without pushing the domain size too far, and to compare results with semi-analytical estimates. Therefore, we investigate differently arranged sphere packings (Simple Cubic (SC), Body-Centered Cubic (BCC), Face-Centered Cubic (FCC)) for a sweep over a wide range for the porosity $\phi = \{0.1, 0.2, 0.3, 0.4, 0.5, 0.6, 0.7, 0.8, 0.9\}$. In addition, all simulations are run at three different resolutions $L/dx = \{60, 100, 200\}$. The results are compared with permeability estimates k_1^{KC} by the semi-analytical, semi-empirical Kozeny-Carman equation (15, 31) (Eq. 11) where D, c_{KC} are the sphere diameter and the Kozeny-Carman constant for which the value $c_{KC} = 180$ is set. In addition, the Stokes solution is further compared with results from a SPH solver that performs simulations based on weakly compressible Navier-Stokes equations (41) (Fig. 6).

$$k_1^{KC} = \frac{D^2}{c_{KC}} \frac{\phi^3}{(1 - \phi)^2} \tag{11}$$

The results from the two solvers, as well as their comparison with the semi-analytical solution, show an almost perfect match. It can be concluded that the solver is capable for a wide range of porosities. A single simulation for a resolution of L/dx = 100 takes an average of 40 minutes on a desktop PC using 4 cores (11th Gen Intel(R) Core(TM) i7-11700KF @ 3.60GHz).

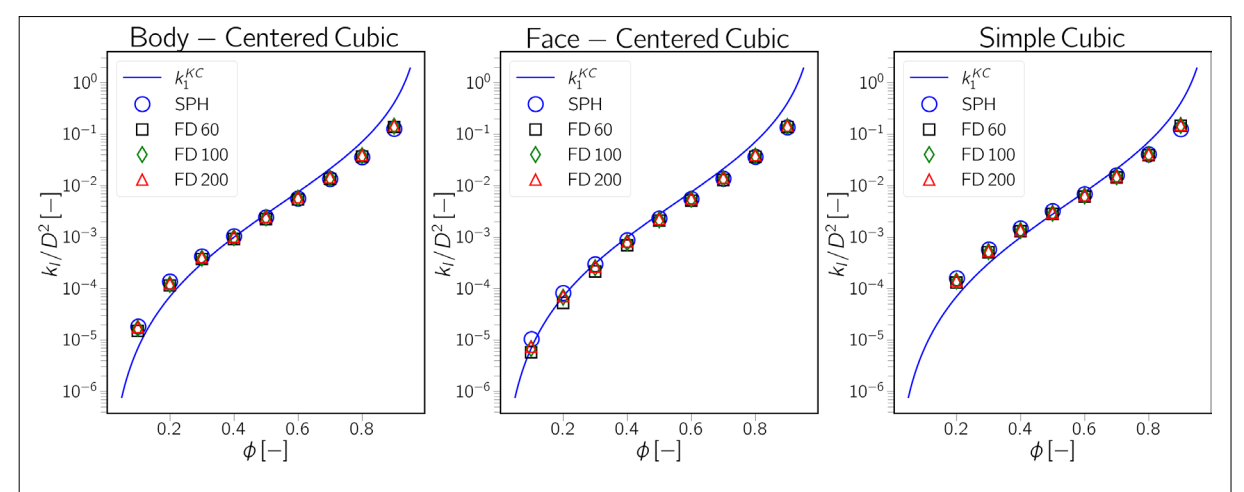


Figure 6: Comparison of Stokes solver results of normalized permeabilities with Karman-Cozeny equation and SPH solver.

6.4. Permeability Tensor and Principal Permeabilities

To compute the anisotropic permeability behavior of various materials, we must not only consider standard benchmarks as well as those for simple porous materials, but also include benchmarks with known or adjustable principal directions. For this purpose, we create a cube with 100^3 voxels corresponding to 1 mm³ and place an ellipsoid in the center. It has the following semi-axes in Cartesian coordinates e_i each given in absolute voxel numbers: $e_1 : a = 35$; $e_2 : b = 10$; $e_3 : c = 35$. By using

Krach, et al Page 11 of 21

this per se periodic structure, one does not have to consider the difficulties that would arise from symmetrical or translational periodization (22). We rotate the single ellipsoid around e_1 -axis in 5° steps for $0^{\circ} \leq \alpha \leq 90^{\circ}$ and compute fluid flow and permeability, whereby the consideration of the permeability in e_1 -direction does not play a role in our evaluation for the time being. As a result, computing the permeability tensor in **Equation 1** is simplified to a two-dimensional problem, where the eigenvalues and principal directions can be represented by an ellipse. Each simulation of a domain described above allows us to determine one column of the coefficient matrix k_{ij} of the permeability tensor, or in our simplified case two entries. The other two entries are obtained from the simulation for which the direction of the imposed pressure gradient relative to the ellipsoid is rotated by 90°. Since the pressure gradient is always applied by the solver in the e_3 -direction, the geometry has to be rotated accordingly, which leads to the exact same result. For instance, considering a rotation of $\alpha^1 = 20^{\circ}$ and consequently $\alpha^2 = -70^{\circ}$, as shown in **Figure 7**, results in the following coefficient matrix for the permeability tensor (**Eq. 12**):

$$k_{ij} = \begin{bmatrix} 1.18 & 0.228 \\ 0.238 & 1.76 \end{bmatrix} \cdot 10^{-7} \text{m}^2 \approx \begin{bmatrix} 1.18 & 0.233 \\ 0.233 & 1.76 \end{bmatrix} \cdot 10^{-7} \text{m}^2$$
 (12)

And finally, we receive the coefficient matrix for the principal axes system (Eq. 13):

$$\tilde{k}_{ij} = \begin{bmatrix} 1.10 & 0\\ 0 & 1.84 \end{bmatrix} \cdot 10^{-7} \text{m}^2 \tag{13}$$

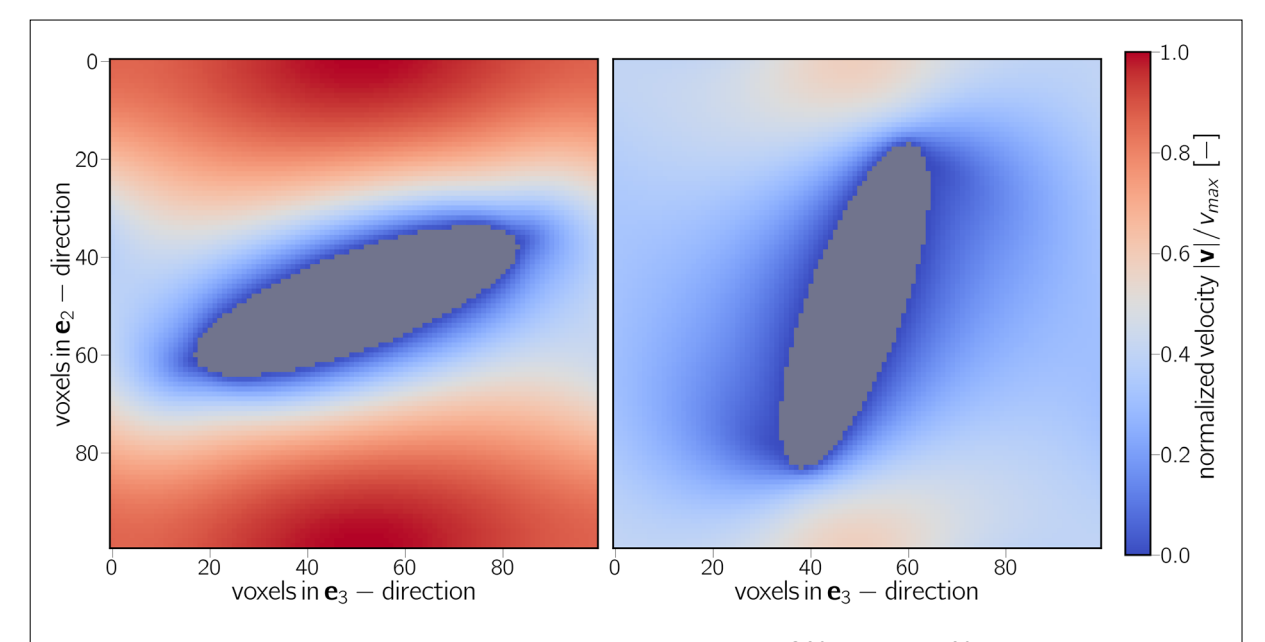
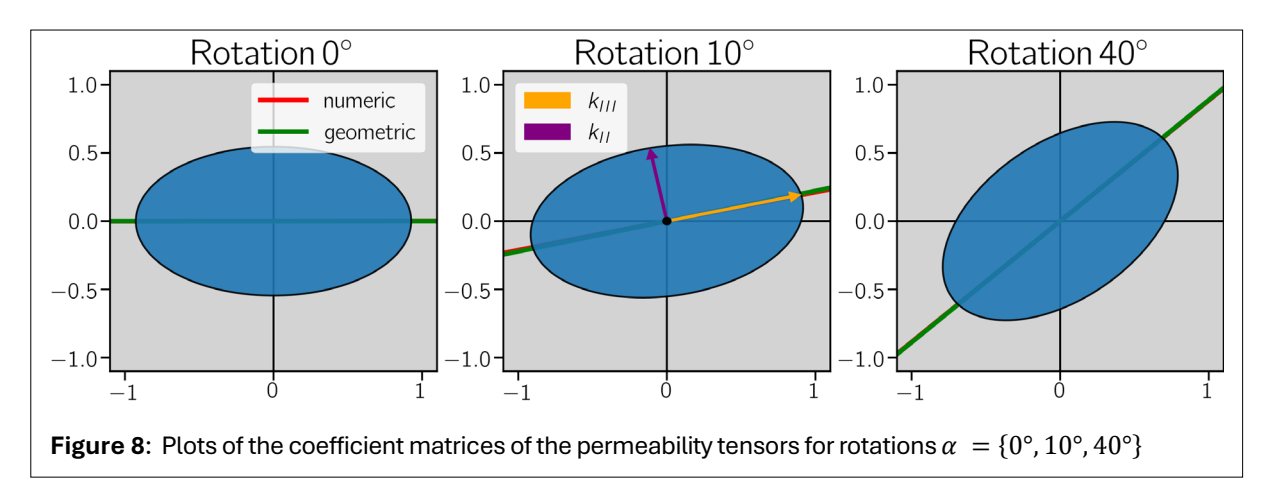


Figure 7: Normalized magnitude of velocity around an ellipsoid with 20° (left) and 70° inclination (right). The same pressure gradient in \mathbf{e}_3 -direction is applied, which explains differences in the maximum velocities. Both figures show a cross-section ($\mathbf{e}_2 - \mathbf{e}_3$ plane) in the center of the domain.

Numerical calculations yield slightly different values for the two corresponding diagonal elements, necessitating a symmetrization in a subsequent step $\left(k_{12} \coloneqq k_{21} = \frac{1}{2}(k_{12} + k_{21})\right)$. In this reduced case, the angle φ between the axes in the original basis system and the principal directions is computed by **Equation 14**, which matches very well to what was being specified. The listing of all values can be found in **Table 1** and a selection is visualized in **Figure 8**.

$$\varphi = \frac{1}{2} \tan^{-1} \left(\frac{2k_{23}}{k_{22} + k_{33}} \right) = \frac{1}{2} \tan^{-1} \left(\frac{2 \cdot 2.33 \cdot 10^{-8} \text{m}^2}{1.76 \cdot 10^{-7} \text{m}^2 + 1.18 \cdot 10^{-7} \text{m}^2} \right) = 19.5^{\circ}$$
(14)

Krach, et al Page 12 of 21



We observe a clearly recognizable trend for an increase of the permeability k_{22} and decrease of k_{33} with increasing rotation α . Performing the transformation, we obtain the same eigenvalues for the permeability, except for minimal differences, which can be explained by the numerical aspects and issues related to discretization. The calculated angles exhibit only small deviations ($< 0.5^{\circ}$) from the geometrically prescribed angles for all inclinations of the ellipsoid. In **Table 1** all values are listed in an organized manner. For this comparably straightforward benchmark geometry, we can demonstrate the overall effectiveness of the workflow.

Table 1	Table 1: Permeabilities, principal permeabilities and principal directions for all simulations.										
α	[°]	0	5	10	15	20	25	30	35	40	45
k_{33}	$[\cdot 10^{-7} \text{m}^2]$	1.85	1.85	1.83	1.80	1.76	1.72	1.66	1.6	1.54	1.47
k_{22}	$[\cdot 10^{-7} \text{m}^2]$	1.09	1.10	1.12	1.14	1.18	1.23	1.29	1.35	1.41	1.47
k_{23}	$[\cdot 10^{-7} \text{m}^2]$	0.00	0.06	0.12	0.18	0.23	0.28	0.32	0.34	0.36	0.37
k_{III}	$[\cdot 10^{-7} \text{m}^2]$	1.85	1.85	1.85	1.85	1.84	1.84	1.84	1.84	1.84	1.84
k_{II}	$[\cdot 10^{-7} \text{m}^2]$	1.09	1.10	1.10	1.10	1.10	1.11	1.11	1.11	1.11	1.11
φ	[°]	0.06	4.73	9.53	14.5	19.5	24.6	29.6	34.7	39.9	45.0

6.5. Testing Against Other Codes

6.5.1. Regular thin, porous media (2D microfluidic devices)

In Section 7.3 we investigate structures that have a small thickness compared to their lateral dimensions. The dimensions of such thin ("2D") porous materials, which are often used in microfluidic characterization of porous media flow, pose problems for numerical methods in terms of efficiency and convergence. To ensure the applicability of the solver for such requirements, we compare it with benchmarks for regular 2D porous materials described in (56). The dimension of the simulated unit cell is 1 mm \times 0.091 mm \times 1 mm and is discretized by 250 \times 27 \times 250 voxels, with a solid frame of two thick voxels each, included in the \mathbf{e}_2 -direction. All results align with the solutions provided in the benchmark paper (**Table 2**).

To illustrate the performance of the solver, the SPH solver used in Wagner et al. (56) needs approximately 17 hours on a 4-core CPU, whereas the presented Stokes solver at the same resolution and on same hardware takes approximately 10 minutes (Table 3).

Table 2: Comparison with different types of pore-scale solvers (SPH, FEM, LBM from Wagner et al. (56)) for thin porous media samples and comparison of computed permeabilities.

Radius	φ	k_{11} range (56)	k_{11} (POREMAPS)
0.35 mm	0.62	$22.9 - 26.7 \cdot 10^{-10} \text{m}^2$	$26.1 \cdot 10^{-10} \text{m}^2$
0.40 mm	0.50	$16.4 - 17.7 \cdot 10^{-10} \text{m}^2$	$17.5 \cdot 10^{-10} \text{m}^2$
0.45 mm	0.36	$7.54 - 8.59 \cdot 10^{-10} \text{m}^2$	$8.08 \cdot 10^{-10} \text{m}^2$
0.47 mm	0.31	$3.62 - 5.35 \cdot 10^{-10} \text{m}^2$	$3.83 \cdot 10^{-10} \text{m}^2$
0.49 mm	0.25	$0.46 - 0.54 \cdot 10^{-10} \text{m}^2$	$0.39 \cdot 10^{-10} \text{m}^2$

Krach, et al Page 13 of 21

Table 3: Properties for different types of 3D benchmarks (range of LBM results from Saxena et al. (49)) and comparison of computed permeabilities.					
Sample	φ	Voxel size	Domain size	k ₁₁ (49)	k_{11} (POREMAPS)
Sphere packing	0.34	7.0 μm	788 × 791 × 793	$2.438 - 2.903 \cdot 10^{-10} \mathrm{m}^2$	$2.512 \cdot 10^{-10} \text{m}^2$
Berea	0.18	2.114 μm	1024 × 1024 × 1024	$4.569 - 6.889 \cdot 10^{-13} \text{m}^2$	$5.772 \cdot 10^{-13} \text{m}^2$
Fontainebleau	0.09	2.072 μm	1024 × 1024 × 1024	$0.642 - 1.411 \cdot 10^{-13} \text{m}^2$	$9.200 \cdot 10^{-14} \text{m}^2$

6.5.2. Irregular sphere packings and porous rock

There are several benchmark papers providing suitable geometries (2, 3, 49). The solver is compared with different 3D benchmarks where permeabilities are computed with, among others, different LBM solvers (49). We computed the sphere packing, one Berea sandstone (Rock1), and one Fontainebleau sandstone (Rock3) sample. The characteristics of the geometries and a comparison of the computed permeabilities k_{11} are summarized in **Table 3**. The results for k_{11} are in accordance with the solutions determined by LBM and thus we consider the benchmarking to be successful and completed.

7. APPLICATIONS

In this section, three different application scenarios are shown to demonstrate the capabilities of POREMAPS. We discuss the range of the solver in terms of (1) the maximum size of the individual simulations and the possibility of (2) investigations into transient effects using simulation campaigns. The solver is applied in areas where the complete permeability tensor cannot be determined experimentally and where the computational effort is substantial. The corresponding domain sizes and computational times are summarized in **Table 4**.

Table 4: Overview of computation times of considered application examples.				
Domain size	Hardware and resources	Computation time		
Example 1 "Berea" and "Sphere packing" (Sect. 6.5 and Sect. 7.1)				
2048 × 2048 × 2048	SimTech Cluster 2, Nodes	36 hrs.		
1576 × 1582 × 1586	SimTech Cluster 2, Nodes	24 hrs.		
3152 × 3164 × 3172	SimTech Cluster 4, Nodes	≈80 hrs.		
Example 2 "Open-cell foam ($\varepsilon_{33}=0.0$ and $\varepsilon_{33}=-0.5$)" (Sect. 7.2)				
800 × 800 × 1186	SimTech Cluster 4, Nodes	8 hrs.		
800 × 800 × 526	SimTech Cluster 4, Nodes	3 hrs.		
Example 3 "Calcite precipitation" (Sect. 7.3)				
12 × 1200 × 1200	SimTech Cluster 1, Node	0.5-2 hrs.		

7.1. Characterization of Large 3D Images

The solver is primarily designed to analyze large, high-resolved 3D images of porous materials typically acquired by 3D imaging methods such as $\mu XRCT$ (45, 52, 64) (**Fig. 9**). This allows the digital characterization of porous materials with regard to hydraulic permeability and can be integrated into the imaging workflow as a subsequent standard procedure. In $\mu XRCT$ imaging, the resolution of REVs is often represented by 3D images with more than 1000^3 voxels. High-resolution X-ray flat panel detectors with approximately 3000×3000 pixels and more are no longer uncommon. This means that, in terms of the reconstructed 3D images, they can contain approximately 3000^3 voxels. With appropriate hardware (large memory), the presented code is capable of handling such large 3D images.

To demonstrate this, we use the 3D image of Berea sandstone (1024 ×1024×1024 voxel) and the sphere packing (788 × 791 × 793 voxel) from Saxena et al. (49), both of which were previously used in the benchmark tests, cf. **Table 3**. Both data sets are mirrored in all three spatial directions resulting in 2048 × 2048 voxels and 1576 × 1582 × 1586 voxels. The corresponding computation times are given in **Table 4** for a convergence criterion of $\varepsilon = \frac{\Delta |q_3|}{|q_3|} < 10^{-6}$. The latter data set is mirrored a second time

Krach, et al Page 14 of 21

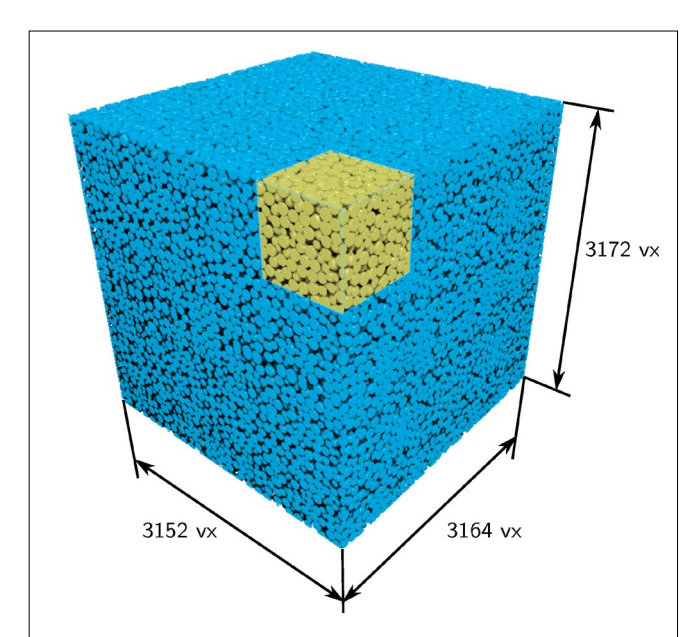


Figure 9: Illustration of the large sized computable domains using the example of a double-mirrored 3D image of a sphere packing (blue) with originally 788 \times 791 \times 793 voxel (yellow). The original 3D image (yellow) is taken from Saxena et al. (49).

in each direction resulting in 3152 \times 3164 \times 3172 voxels (equals 64 times the original geometry), cf. **Figure 9**. Due to parallelized IO routines, this can be implemented using 4 nodes, with a total of 512 cores, requiring a total of \approx 1.5 TB RAM. This encompasses μ XRCT data produced by state-of-the-art high resolution detectors and enables processing without information loss through binning, using a manageable amount of resources.

7.2. Deformation-dependent Permeability and Permeability Anisotropy—Uniaxial Compression of an Open-Cell Foam

The deformation-dependent permeability of open-cell foams has been studied experimentally by several researchers. Various theoretical models have been proposed for predicting the effect of strain on permeability, cf. Dawson, Germaine, and Gibson (19); Markert (37) and therein cited literature. In

experimental studies, uniaxial compression loading is often imposed on a foam sample and the deformation-dependent permeability is measured in one direction, often in the same direction as the imposed load. Measuring the permeability in different directions is technically challenging. Using non-destructive μ XRCT imaging is a potential approach to overcome this problem, provided the fluid-solid interaction is negligible and the foam can be considered rigid at a given deformation state. In this case, the foam structure is imaged under different loading conditions in 3D. The time-series of 3D images, followed by subsequent post-processing, provides the opportunity to conduct virtual experiments and characterize the structure and deformation-dependency in more detail.

This is exemplary shown for an open-cell Polyurethane (PUR) cylindrical foam sample with 10 PPI subjected to uniaxial compressive loading and imaged at discrete loading states (engineering compressive strain $\varepsilon_{33} = -\{0.0, 0.1, 0.2, 0.3, 0.4, 0.5\}$), see **Figure 10a**. For the imaging, the system presented in Ruf and Steeb (45) along with that from Ruf, Lee, and Steeb (44) was employed. For the series of 3D images, the permeability tensor is determined using cubic sub volumes of size $800 \times 800 \times 526-1186$ voxel with a uniform voxel size of 74.8 µm. The permeability tensor (three simulations) for each loading condition is determined in $\approx 3-8$ hrs. The permeability in axial direction (\mathbf{e}_3) and radial directions (\mathbf{e}_1 , \mathbf{e}_2) and the principal values are shown in **Figure 10b** over the applied strain (left) and the foam porosity (right). At all deformation states, the radial permeabilities k_{11} and k_{22} are quite similar and differ slightly from the axial permeability k_{33} of the cylindrical sample. In general, it can be said that the permeability anisotropy does not correlate in a systematic way, neither with the strain nor with the porosity, which contradicts the expectation.

7.3. Anisotropy development during calcite precipitation

Predicting pore-scale clogging phenomena in heterogeneous porous materials presents a significant challenge. These processes can occur inadvertently, and if they cannot be prevented, there is a need to manage them, such as in the case of clogged filters. Conversely, these processes might also be intentional, such as in the case of blocking subsurface cracks. We focus our investigation on a specific

Krach, et al Page 15 of 21

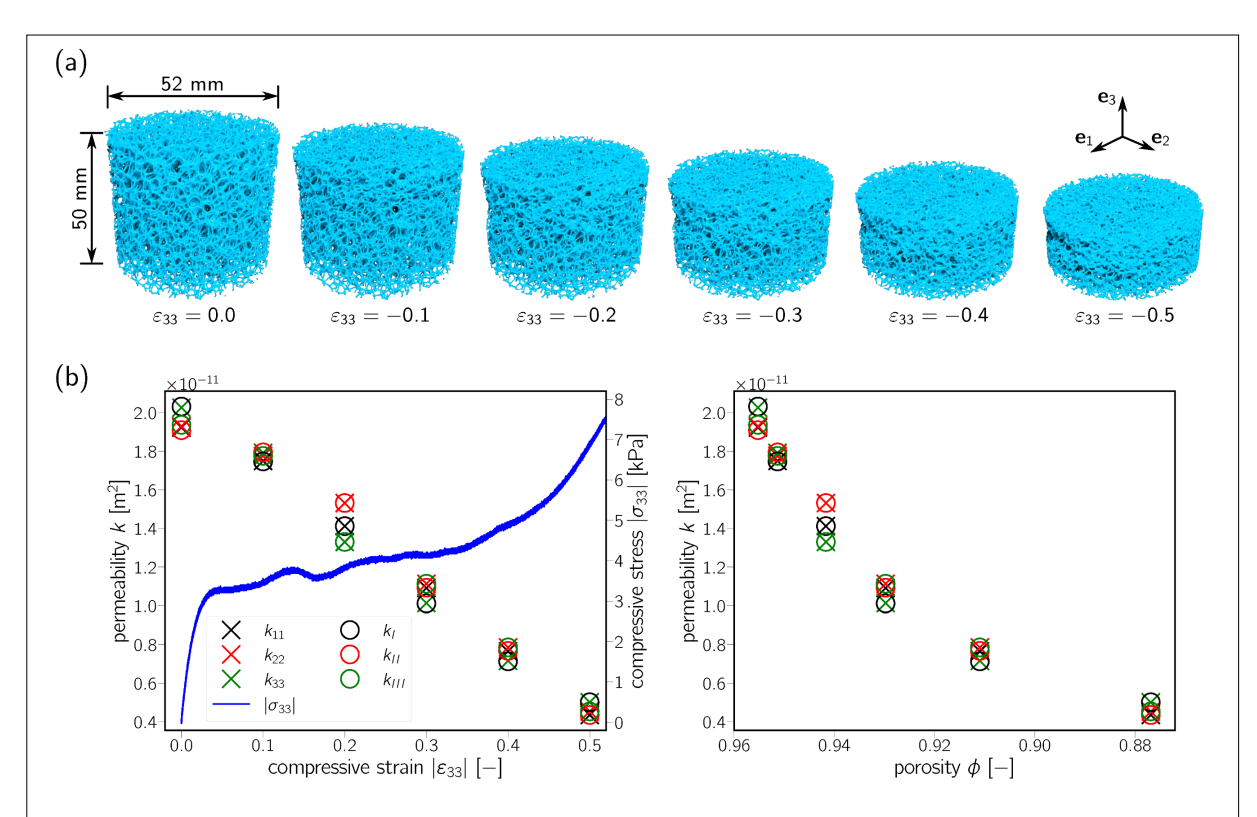


Figure 10: Deformation-dependent permeability and anisotropy of an open-cell PUR foam sample (10 PPI) based on μ XRCT images (46, 47). a) Segmented μ XRCT images for different uniaxial compression loading states. b) Determined permeabilities in \mathbf{e}_1 -, \mathbf{e}_2 -, \mathbf{e}_3 -direction and principle permeabilities.

scenario where pore spaces gradually become obstructed due to a chemically induced precipitation process. The experimental data set (60) serves as the basis for our study, and the details of data acquisition and the experimental arrangement are elaborated upon in Weinhardt et al. (58); Weinhardt (57); Weinhardt, Deng, Hommel, et al. (59). We have already described this procedure of investigation to a smaller extent as a proof of concept in Krach and Steeb (33).

Unlike the experimental procedure, we can determine the permeability k_{33} in the \mathbf{e}_3 -direction (aligned with the pressure gradient in the experiment) and the permeability k_{22} in the \mathbf{e}_2 -direction (perpendicular to the pressure gradient) at various time steps during the experiment. This investigation includes 137 individual simulations, where for 57 time steps the domain is percolating in both directions, resulting in 2 simulations per time step. In the \mathbf{e}_3 -direction, a flow path remains unblocked for a longer time and 80 time steps are investigated. A simulation (12 × 1200 × 1200 voxel) typically runs for an average of 2 hours on a node using 121 CPU-cores. We explicitly fix the domain decomposition to 1 × 11 × 11 ranks.

Two-dimensional image data is used as basis and replicated in the third spatial direction to simulate the original dimensions of the microfluidic experiment in 3D. We are particularly interested in a preferential flow path that forms in the upper region of the domain and stays almost free during the experiment. Accordingly, a subdomain is extracted. In the course of the experiment, more and more precipitate is accumulated in the domain, thus increasing the solid fraction and decreasing porosity and permeability. Figure 11 shows the geometries (black = solid body, gray = precipitate) and the velocity patterns. Note that we simulate the same domain twice with pressure gradient from left to right (\mathbf{e}_3 -direction: Fig. 11, center column) and pressure gradient from top to bottom (\mathbf{e}_2 -direction: Fig. 11, right column). The simulations include all the time steps of the experiment up to the point where there is no flow path through the porous material at all. The material clogs first in the \mathbf{e}_2 -direction, at a porosity of $\phi = 27.7$ %, while a flow path remains open in the \mathbf{e}_3 -direction at this point.

Krach, et al Page 16 of 21

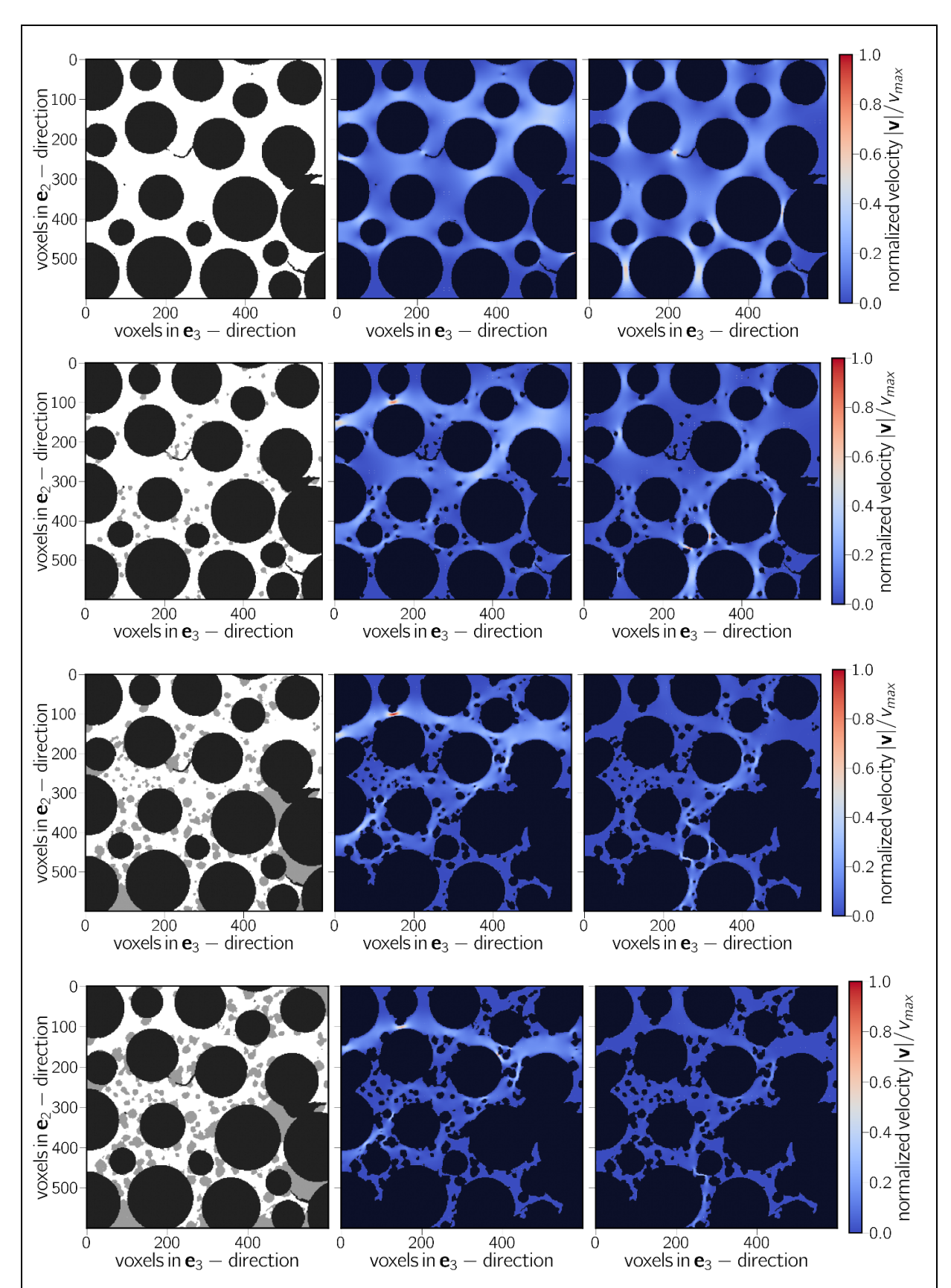


Figure 11: Geometry and flow patterns at different times (increasing from top to bottom) during the experiment. The left column represents the input domain (black - solid columns, gray - precipitate). For the simulations, the precipitates are attributed to the solid. Columns 2 and 3 show the normalized absolute velocities based on pressure gradients in \mathbf{e}_3 - and \mathbf{e}_2 -direction.

Krach, et al Page 17 of 21

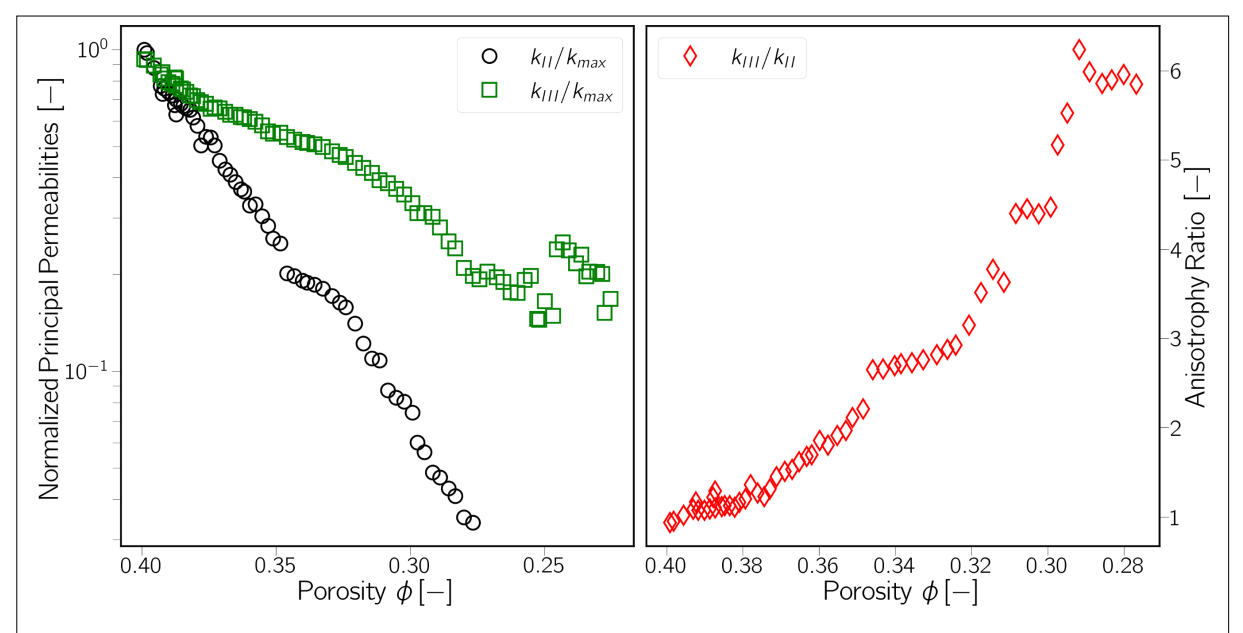


Figure 12: Normalized eigenvalues of the permeability tensor (k_{II} , k_{III}) over the course of a decreasing porosity (left) and the relation of both (k_{III}/k_{II}) illustrating a clear development of anisotropic hydraulic properties (right).

The focus of the analysis lies in the development of the degree of anisotropy in the course of the experiment. For this purpose, the eigenvalues of the 2 × 2 permeability tensor are determined. **Figure 12** shows the eigenvalues k_{II} and k_{III} plotted against the porosity ϕ . The principal permeability k_{II} decreases significantly faster than k_{III} . The degree of anisotropy, represented by the ratio of the eigenvalues $\frac{k_{II}}{k_{III}}$ (**Fig. 12**, right), increases in a stepwise linear fashion during the experiment, reaching a ratio of 6. Thus, this analysis provides an additional benefit that experiments cannot provide.

8. DISCUSSION AND CONCLUSION

The present study introduces POREMAPS, an FDM solver designed for solving steady-state incompressible Stokes equations using the artificial compressibility method. This solver was developed specifically to compute the permeability tensor ${\bf k}$ of arbitrary porous materials. Through a series of benchmarks with increasing complexity, we have demonstrated the solver's robustness and efficiency in handling a wide range of porosities $0.1 < \phi < 0.9$, showcasing its ability to efficiently and reliably process different material types.

Three applications were investigated to further illustrate the solver's versatility and performance. The first application involves large-scale simulations, with voxel numbers reaching > 3000^3 (see Sect. 7.1). This highlights the solver's capacity to manage computationally intensive problems. Additionally, we conducted two extensive simulation campaigns (Sect. 7.2 and 7.3). The first campaign focused on the permeability of open-cell foams under mechanical deformation. Our results indicate that no significant anisotropy in permeability develops even under substantial strain $\varepsilon_{33} = -0.5$, although we observe a reduction in permeability by approximately one order of magnitude. This finding is noteworthy, as we originally expected anisotropy to arise under such conditions. The second campaign studied porous materials prone to clogging, where we quantified the resulting anisotropy ratio k_{III} / k_{II} . In this context, POREMAPS provided insights that would be difficult to achieve experimentally, highlighting one of its key advantages: offering a computational framework to investigate material behavior free from experimental limitations.

Despite the computational and hardware demands associated with large-scale simulations, the solver remains relatively efficient. Furthermore, its ease of use, coupled with seamless integration with

Krach, et al Page 18 of 21

experimental imaging data, positions it as a valuable tool for a wide range of applications in material science and fluid dynamics. We believe that the solver holds significant potential for future research, particularly in areas where experimental approaches may be impractical or limited by scale, which is often the case with anisotropy studies.

STATEMENTS AND DECLARATIONS

Supplementary Material

Information on the Nomenclature, Nondimensional balance equations, Discrete equations and fluid-solid boundary conditions, and the Permeability computation for this paper can be found in the Supplementary Material, which is available online.

Acknowledgements

D.K. and H.S. acknowledge funding from the Deutsche Forschungsgemeinschaft (DFG, German Research Foundation) under Germany's Excellence Strategy - EXC 2075 – 390740016. M.R. and H.S. acknowledge funding from the DFG through the project STE 969/13-1 (Project No. 357361983) and supporting this work within the SFB 1313 (Project No. 327154368). We acknowledge the support by the Stuttgart Center for Simulation Science (SC SimTech).

Author Contributions

D. Krach: Conceptualization, Methodology, Investigation, Software, Validation, Data Curation, Writing, Original Draft, Visualization, Project administration. **M. Ruf:** Investigation, Software, Data Curation, Writing - Original Draft, Writing - Review & Editing, Visualization. **H. Steeb:** Conceptualization, Writing, Review & Editing, Supervision, Funding acquisition.

Conflicts of Interest

The authors declare that they have no known competing financial interests or personal relationships that could have appeared to influence the work reported in this paper.

Data, Code & Protocol Availability

The complete source code including input data of the shown application examples that support the findings of this study is openly available in the Data Repository of the University of Stuttgart (DaRUS) at https://doi.org/10.18419/darus-3676 (32).

Funding Received

D.K. and H.S. acknowledge funding from the Deutsche Forschungsgemeinschaft (DFG, German Research Foundation) under Germany's Excellence Strategy - EXC 2075 – 390740016. M.R. and H.S. acknowledge funding from the DFG through the project STE 969/13-1 (Project No. 357361983) and supporting this work within the SFB 1313 (Project No. 327154368).

ORCID IDs

REFERENCES

- 1. Adler, P. M., Jacquin, C. G., & Quiblier, J. A. (1990). Flow in simulated porous media. *International Journal of Multiphase Flow*, 16(4), 691–712. https://doi.org/10.1016/0301-9322(90)90025-E
- Andrä, H., Combaret, N., Dvorkin, J., Glatt, E., Han, J., et al. (2013a). Digital rock physics benchmarks—Part I: Imaging and segmentation. *Computers & Geosciences*, 50, 25–32. https://doi.org/10.1016/j.cageo.2012.09.005

Krach, et al Page 19 of 21

3. Andrä, H., Combaret, N., Dvorkin, J., Glatt, E., Han, J., et al. (2013b). Digital rock physics benchmarks—part II: Computing effective properties. *Computers & Geosciences*, 50, 33–43. https://doi.org/10.1016/j.cageo.2012.09.008

- 4. Aziz, K., & Wong, T. (1989). Considerations in the development of multipurpose reservoir simulation models. In: *Proceedings of the First and Second Forum on Reservoir Simulation*, Alpbach, pp. 77–208.
- 5. Bakhshian, S., & Sahimi, M. (2016). Computer simulation of the effect of deformation on the morphology and flow properties of porous media. *Physical Review E*, 94(4), 042903. https://doi.org/10.1103/PhysRevE.94.042903
- 6. Batchelor, G. K. (1967). *An Introduction to Fluid Dynamics*. Cambridge University Press. Bear, J. (1988). Dynamics of Fluids in Porous Media. Dover.
- 7. Bear, J., & Verruijt, A. (1987). *Modeling Groundwater Flow and Pollution*. Springer Science & Business Media.
- 8. Bentz, D., & Martys, N. (2007). A Stokes Permeability Solver for Three-Dimensional Porous Media (Techreport No. NISTIR 7416). https://nvlpubs.nist.gov/nistpubs/Legacy/IR/nistir7416.pdf
- 9. Bernard, D., Nielsen, Ø., Salvo, L., & Cloetens, P. (2005). Permeability assessment by 3D interdendritic flow simulations on microtomography mappings of Al–Cu alloys. *Materials Science and Engineering: A*, 392(1–2), 112–120. https://doi.org/10.1016/j.msea.2004.09.004
- 10. Blunt, M. J. (2017). Multiphase flow in permeable media (1st ed). Cambridge University Press.
- 11. Blunt, M. J., Bijeljic, B., Dong, H., Gharbi, O., Iglauer, S., et al. (2013). Pore-scale imaging and modelling. *Advances in Water Resources*, 51, 197–216. https://doi.org/10.1016/j.advwatres.2012.03.003
- 12. Borujeni, A. T., Lane, N. M., Thompson, K., & Tyagi, M. (2013). Effects of image resolution and numerical resolution on computed permeability of consolidated packing using LB and FEM pore-scale simulations. *Computers & Fluids*, 88, 753–763. https://doi.org/10.1016/j.compfluid.2013.05.019
- 13. Burger, W., & Burge, M. J. (2016). *Digital image processing: An algorithmic introduction using java* (2nd ed. 2016). Springer London: Imprint: Springer.
- Cantisano, M. T., Restrepo, D. P., Cespedes, S., Toelke, J., Grader, A., Suhrer, M., & Walls, J. (2013). Relative permeability in a shale formation in Colombia using digital rock physics. *Unconventional Resources Technology Conference*, Denver, Colorado, 12-14 August 2013, 909–915. https://doi.org/10.1190/urtec2013-092
- 15. Carman, P. C. (1997). Fluid flow through granular beds. *Chemical Engineering Research and Design*, 75, S32–S48. https://doi.org/10.1016/S0263-8762(97)80003-2
- 16. Chareyre, B., Cortis, A., Catalano, E., & Barthélemy, E. (2012). Pore-scale modeling of viscous flow and induced forces in dense sphere packings. *Transport in Porous Media*, 94(2), 595–615. https://doi.org/10.1007/s11242-012-0057-2
- 17. Chorin, A. J. (1967). A numerical method for solving incompressible viscous flow problems. *Journal of Computational Physics*, 2(1), 12–26. https://doi.org/10.1016/0021-9991(67)90037-X
- 18. Darcy, H. (1856). Les fontaines publiques de la ville de Dijon: Exposition et application des principes à suivre et des formules à employer dans les questions de distribution d'eau. Paris: Victor Dalmont.
- Dawson, M. A., Germaine, J. T., & Gibson, L. J. (2007). Permeability of open-cell foams under compressive strain. *International Journal of Solids and Structures*, 44(16), 5133–5145. https://doi.org/10.1016/j.ijsolstr.2006.12.025
- 20. Dong, H., & Blunt, M. J. (2009). Pore-network extraction from micro-computerized-tomography images. *Physical Review E*, 80(3), 036307. https://doi.org/10.1103/PhysRevE.80.036307
- 21. Gerke, K. M., Vasilyev, R. V., Khirevich, S., Collins, D., Karsanina, M. V., et al. (2018). Finite-difference method Stokes solver (FDMSS) for 3D pore geometries: Software development, validation and case studies. *Computers & Geosciences*, 114, 41–58. https://doi.org/10.1016/j.cageo.2018.01.005
- 22. Guibert, R., Horgue, P., Debenest, G., & Quintard, M. (2016). A comparison of various methods for the numerical evaluation of porous media permeability tensors from pore-scale geometry. *Mathematical Geosciences*, 48(3), 329–347. https://doi.org/10.1007/s11004-015-9587-9
- 23. Harlow, F. H., & Welch, J. E. (1965). Numerical calculation of time-dependent viscous incompressible flow of fluid with free surface. *The Physics of Fluids*, 8(12), 2182–2189. https://doi.org/10.1063/1.1761178
- 24. Helmig, R. (1997). *Multiphase Flow and Transport Processes in the Subsurface: A Contribution to the Modeling of Hydrosystems.* Springer-Verlag.
- 25. Hilliard, Z., Evans, T. M., & Peszynska, M. (2024). Modeling flow and deformation in porous media from porescale to the Darcy-scale. *Results in Applied Mathematics*, 22, 100448. https://doi.org/10.1016/j.rinam.2024.100448

Krach, et al Page 20 of 21

26. Holmes, D. W., Williams, J. R., Tilke, P., & Leonardi, C. R. (2016). Characterizing flow in oil reservoir rock using SPH: Absolute permeability. *Computational Particle Mechanics*, 3(2), 141–154. https://doi.org/10.1007/s40571-015-0038-7

- 27. Hommel, J., Gehring, L., Weinhardt, F., Ruf, M., & Steeb, H. (2022). Effects of enzymatically induced carbonate precipitation on capillary pressure–saturation relations. *Minerals*, 12(10), 1186. https://doi.org/10.3390/min12101186
- 28. Iassonov, P., Gebrenegus, T., & Tuller, M. (2009). Segmentation of X-ray computed tomography images of porous materials: A crucial step for characterization and quantitative analysis of pore structures. *Water Resources Research*, 45(9), 2009WR008087. https://doi.org/10.1029/2009WR008087
- 29. Icardi, M., Boccardo, G., Marchisio, D. L., Tosco, T., & Sethi, R. (2014). Pore-scale simulation of fluid flow and solute dispersion in three-dimensional porous media. *Physical Review E*, 90(1), 013032. https://doi.org/10.1103/PhysRevE.90.013032
- 30. Jiang, F., & Tsuji, T. (2014). Changes in pore geometry and relative permeability caused by carbonate precipitation in porous media. *Physical Review E*, 90(5), 053306. https://doi.org/10.1103/PhysRevE.90.053306
- 31. Kozeny, J. (1927). Über die kapillare Leitung des Wassers im Boden. *Sitzungberichte, Mathematik, Astronomie, Physik und Meteorologie,* 136(2a), 271–306.
- 32. Krach, D., Ruf, M., & Steeb, H. (2024). POREMAPS 1.0.0: Code, Benchmarks, Applications. DaRUS. https://doi.org/10.18419/DARUS-3676
- 33. Krach, D., & Steeb, H. (2023). Comparing methods for permeability computation of porous materials and their limitations. *PAMM*, 23(1), e202200225. https://doi.org/10.1002/pamm.202200225
- 34. Lemaitre, R., & Adler, P. M. (1990). Fractal porous media IV: Three-dimensional stokes flow through random media and regular fractals. *Transport in Porous Media*, 5(4), 325–340. https://doi.org/10.1007/BF01141990
- 35. Liao, Q., Wei, Z., Yan, Z., You, S., Cui, M., et al. (2024). Parallelizable permeability estimation of digital porous media for sandstone using subvolume properties for flow in porous media. *Journal of Energy Engineering*, 150(5), 04024023. https://doi.org/10.1061/JLEED9.EYENG-5390
- 36. Liu, J., Pereira, G. G., & Regenauer-Lieb, K. (2014). From characterisation of pore-structures to simulations of pore-scale fluid flow and the upscaling of permeability using microtomography: A case study of heterogeneous carbonates. *Journal of Geochemical Exploration*, 144, 84–96. https://doi.org/10.1016/j.gexplo.2014.01.021
- 37. Markert, B. (2007). A constitutive approach to 3-D nonlinear fluid flow through finite deformable porous continua: With application to a high-porosity polyurethane foam. *Transport in Porous Media*, 70(3), 427–450. https://doi.org/10.1007/s11242-007-9107-6
- 38. Math2Market GmbH, Becker, J., Biebl, F., Cheng, L., Glatt, E., et al. (2023). GeoDict Releases 2023. Math2Market GmbH. https://doi.org/10.30423/release.geodict2023
- 39. Message Passing Interface Forum. (2021). MPI: A message-passing interface standard version 4.0. Retrieved from https://www.mpi-forum.org/docs/mpi-4.0/mpi40-report.pdf
- 40. Noiriel, C., Steefel, C. I., Yang, L., & Bernard, D. (2016). Effects of pore-scale precipitation on permeability and flow. *Advances in Water Resources*, 95, 125–137. https://doi.org/10.1016/j.advwatres.2015.11.013
- 41. Osorno, M., Schirwon, M., Kijanski, N., Sivanesapillai, R., Steeb, H., & Göddeke, D. (2021). A cross-platform, high-performance SPH toolkit for image-based flow simulations on the pore scale of porous media. *Computer Physics Communications*, 267, 108059. https://doi.org/10.1016/j.cpc.2021.108059
- 42. Peyret, R., & Taylor, T. D. (1983). Computational methods for fluid flow. Springer Berlin Heidelberg. https://doi.org/10.1007/978-3-642-85952-6
- 43. Piovesan, A., Achille, C., Ameloot, R., Nicolai, B., & Verboven, P. (2019). Pore network model for permeability characterization of three-dimensionally-printed porous materials for passive microfluidics. *Physical Review E*, 99(3), 033107. https://doi.org/10.1103/PhysRevE.99.033107
- 44. Ruf, M., Lee, D., & Steeb, H. (2023). A multifunctional mechanical testing stage for micro x-ray computed tomography. *Review of Scientific Instruments*, 94(8), 085115. https://doi.org/10.1063/5.0153042
- 45. Ruf, M., & Steeb, H. (2020). An open, modular, and flexible micro X-ray computed tomography system for research. *Review of Scientific Instruments*, 91(11), 113102. https://doi.org/10.1063/5.0019541
- 46. Ruf, M., & Steeb, H. (2024). In situ micro-XRCT data set of an open-cell polyurethane foam sample under uniaxial compression load. DaRUS. https://doi.org/10.18419/DARUS-3010
- 47. Ruf, M., Steeb, H., & Karadimitriou, N. (2023). Visualization of the uniaxial compression of open-cell foams. In: *Album of Porous Media: Structure and Dynamics*, pp. 117–117. Springer.
- 48. Russ, J. C., & Neal, F. B. (2018). The image processing handbook (0 ed.). CRC Press. https://doi.org/10.1201/b18983

Krach, et al Page 21 of 21

49. Saxena, N., Hofmann, R., Alpak, F. O., Berg, S., Dietderich, J., et al. (2017). References and benchmarks for pore-scale flow simulated using micro-CT images of porous media and digital rocks. *Advances in Water Resources*, 109, 211–235. https://doi.org/10.1016/j.advwatres.2017.09.007

- 50. Scheidegger, A. E. (1957). The Physics of Flow through Porous Media. University of Toronto press.
- 51. Schlüter, S., Sheppard, A., Brown, K., & Wildenschild, D. (2014). Image processing of multiphase images obtained via X-ray microtomography: A review. *Water Resources Research*, 50(4), 3615–3639. https://doi.org/10.1002/2014WR015256
- 52. Stock, S. R. (2018). Microcomputed tomography: Methodology and applications (1st ed.). CRC Press. https://doi.org/10.1201/9781420058772
- 53. Tartakovsky, A. M., Trask, N., Pan, K., Jones, B., Pan, W., & Williams, J. R. (2016). Smoothed particle hydrodynamics and its applications for multiphase flow and reactive transport in porous media. *Computational Geosciences*, 20(4), 807–834. https://doi.org/10.1007/s10596-015-9468-9
- 54. Thomas, M., & Corry, B. (2016). A computational assessment of the permeability and salt rejection of carbon nanotube membranes and their application to water desalination. *Philosophical Transactions of the Royal Society A: Mathematical, Physical and Engineering Sciences*, 374(2060), 20150020. https://doi.org/10.1098/rsta.2015.0020
- 55. Tuller, M., Kulkarni, R., & Fink, W. (2015). Segmentation of X-ray CT data of porous materials: A review of global and locally adaptive algorithms. In S. H. Anderson & J. W. Hopmans (Eds.), SSSA Special Publications (pp. 157–182). American Society of Agronomy and Soil Science Society of America. https://doi.org/10.2136/sssaspecpub61.c8
- 56. Wagner, A., Eggenweiler, E., Weinhardt, F., Trivedi, Z., Krach, D., et al. (2021). Permeability estimation of regular porous structures: A benchmark for comparison of methods. *Transport in Porous Media*, 138(1), 1–23. https://doi.org/10.1007/s11242-021-01586-2
- 57. Weinhardt, F. (2022). Porosity and permeability alterations in processes of biomineralization in porous media—Microfluidic investigations and their interpretation. Universität Stuttgart. https://doi.org/10.18419/OPUS-12822
- 58. Weinhardt, F., Class, H., Vahid Dastjerdi, S., Karadimitriou, N., Lee, D., & Steeb, H. (2021). Experimental methods and imaging for enzymatically induced calcite precipitation in a microfluidic cell. *Water Resources Research*, 57(3), e2020WR029361. https://doi.org/10.1029/2020WR029361
- 59. Weinhardt, F., Deng, J., Hommel, J., Vahid Dastjerdi, S., Gerlach, R., Steeb, H., & Class, H. (2022). Spatiotemporal distribution of precipitates and mineral phase transition during biomineralization affect porosity–permeability relationships: Microfluidic investigations. *Transport in Porous Media*, 143(2), 527–549. https://doi.org/10.1007/s11242-022-01782-8
- 60. Weinhardt, F., Deng, J., Steeb, H., & Class, H. (2022). Optical microscopy and log data of enzymatically induced calcite precipitation (EICP) in microfluidic cells (Quasi-2D-structure). *DaRUS*. https://doi.org/10.18419/DARUS-1799
- 61. White, F. M., & Majdalani, J. (2006). Viscous Fluid Flow. McGraw-Hill New York.
- 62. Wildenschild, D., & Sheppard, A. P. (2013). X-ray imaging and analysis techniques for quantifying pore-scale structure and processes in subsurface porous medium systems. *Advances in Water Resources*, 51, 217–246. https://doi.org/10.1016/j.advwatres.2012.07.018
- 63. Wildenschild, D., Vaz, C. M. P., Rivers, M. L., Rikard, D., & Christensen, B. S. B. (2002). Using X-ray computed tomography in hydrology: Systems, resolutions, and limitations. *Journal of Hydrology*, 267(3–4), 285–297. https://doi.org/10.1016/S0022-1694(02)00157-9
- 64. Withers, P. J., Bouman, C., Carmignato, S., Cnudde, V., Grimaldi, D., Hagen, C. K., Maire, E., Manley, M., Du Plessis, A., & Stock, S. R. (2021). X-ray computed tomography. *Nature Reviews Methods Primers*, 1(1), 18. https://doi.org/10.1038/s43586-021-00015-4